The Combined Influence of Rotation and Scrape-Off Layer Drifts on Recycling Asymmetries in Tokamak Plasmas

E.D Emdee[1], L. Horvath[1], A. Bortolon[1], R. Gerrú[2], G.J Wilkie[1], S. Haskey[1], and F. Laggner[3]
[1]*Princeton Plasma Physics Laboratory, Princeton, NJ 08543, USA*
[2]*Massachusetts Institute of Technology, Plasma Science and Fusion Center, Cambridge, MA 02139, United States of America and*
[3]*North Carolina State University, Raleigh, NC, United States of America*

Coupled 2D fluid-kinetic simulations of a DIII-D high confinement tokamak plasma show that plasma rotation coupled with drift effects near the plasma edge plays a significant role in the creation of the observed poloidal distribution of neutrals. It is observed that including either drift or rotation effects enhances particle flux at the inner target in the case of ion B×∇B drift towards the X-point. However, the particle flux asymmetry is significantly higher with the combination of drifts and rotation, than either effect alone. The observed heightened particle flux asymmetry allows for improved simulation of the strong in-out asymmetry of the Lyman-α brightness profiles measured in the experiment. Enhancement of radial transport of parallel momentum changes the upstream scrape-off layer flow pattern, increasing the fraction of deuterium flux that reaches the inboard divertor entrance while lowering that which arrives at the outboard. This work indicates that by combining drifts, rotation and viscous coupling, existing boundary plasma models can achieve a satisfactory agreement with experimentally measured neutral asymmetries.

Understanding the mechanisms that generate and sustain the density pedestal of tokamaks' high-confinement plasma is necessary to successfully design future fusion reactors [1]. The density pedestal forms by the combined action of local particle fueling and transport. The fueling is associated with ionization of neutral atoms from the region surrounding the plasma volume and tends to generate a steep density gradient near the plasma edge. Although the relative roles of transport and fueling remain an open question [2], it is generally accepted that neutral fueling plays a major role in present-day devices [3]. Since fueling neutrals arise largely from plasma flux neutralized at the divertor targets, a process known as recycling, understanding what drives this flux of ions to the targets is of paramount importance.

Cross field drifts are often cited as the primary physical mechanism for asymmetries frequently observed in divertor electron density, namely the particle drift due to an electric field, $\vec{V}_{E\times B} = \frac{\vec{E}\times\vec{B}}{B^2}$. Given the magnetic geometry of a tokamak, this flow provides flow from the outer Low Field Side (LFS) divertor to the inner High Field Side (HFS) divertor via the Private Flux Region (PFR) for a configuration with toroidal magnetic field counterclockwise looking from above the torus, more commonly stated as ion B×∇B into the lower divertor [4, 5]. This electric field arises through a variety of physical mechanisms, though, in the high confinement mode (H-mode) plasma which is the focus of this Letter, it is generally thought to be strongly influenced by turbulent Reynolds stress and ion polarization effects [6, 7], with possible contributions from finite ion orbit width effects [8].

In this Letter we demonstrate how rotation of a magnetically confined tokamak plasma can affect the asymmetry of particle flux to the divertor via viscous coupling of edge and core plasma flow. The connection between upstream rotation and the divertor has been considered as a potential mechanism for particle flux asymmetries in the past [9], but never demonstrated with a high fidelity physics code as shown here. Specifically, we present interpretative simulations of a DIII-D tokamak experiment showing that, by accounting for the experimentally observed upstream plasma rotation, significant changes are observed in the asymmetry of inner (HFS) and outer (LFS) divertor target flux. The combined effect of rotation and drifts is determined to be significantly greater than the additive effects of either alone, indicating an emergent property of the momentum transport.

First-principle gyrokinetic simulations of a DIII-D H-mode plasma [10] found that the plasma flows in the Scrape-Off Layer (SOL) play an important role in generating the inboard/outboard asymmetry of pedestal ionization sources comparable with the experiment [11, 12]. These SOL poloidal flows are the combination of both drift flows and flow parallel to the magnetic field, projected into the poloidal plane. In the absence of extrinsic torques, viscous coupling with the SOL plasma can give rise to these parallel flows within the confined plasma [13–15]. Previous work has noted that low-torque plasma SOL rotation may be self-generated due to poloidal E×B flows and the resulting poloidal pressure asymmetries [16]. Vice versa, core plasma rotation can be expected to overwhelm the intrinsic momentum generation and strongly influence the SOL flows in the presence of strong applied torque, e.g. from neutral beams [17]. The simulations presented here demonstrate that this coupling has important implications for target recycling.

The simulations focus on an H-mode deuterium plasma (B_T=2 T, I_p=1.2 MA), with ion ∇B drift directed towards the X-point. In the time of interest, t∼3.0-4.0 s, the plasma was quasi-stationary, with 2.8 MW of neutral

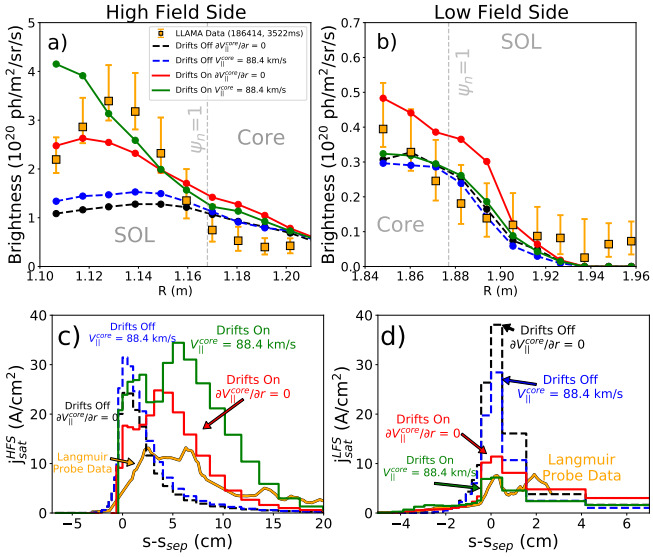

FIG. 1. a) HFS and b) LFS Lyman-α brightness measured by LLAMA (orange) compared to four different SOLPS cases' synthetic diagnostic. c) HFS and d) LFS comparison of target saturation current in the same simulations, compared to Langmuir probe data from a shot with similar parameters (shot #184554, time averaged across 3300 ms±300 ms).

beam heating and with no external gas injection. As such the plasma fueling was provided by wall recycling and, to a lesser extent, wall desorption. In this experiment the edge fueling was measured with the LLAMA diagnostic [12]. Ly-α brightness is measured at locations across the inboard and outboard separatrix (shown in Fig. 2a). Fig. 1a and 1b show the radial profiles of Ly-α brightness measured by LLAMA, demonstrating a strong HFS/LFS asymmetry, with a factor of 9 difference in peak brightness. Fig. 1c and 1d show that HFS/LFS asymmetry in the saturation current is observed via Langmuir probes as well for this configuration. A different discharge with similar parameters was used specifically for the Langmuir probe data, due to Langmuir probe measurements being unavailable for the simulated discharge.

The simulations were carried out with the SOLPS-ITER code, a coupled 2D fluid kinetic model which combines the plasma fluid code B2.5 with the Monte Carlo neutral code EIRENE [18]. The simulations presented here have two ion species, carbon and deuterium. SOLPS requires user-defined, radially varying, anomalous transport diffusivities to determine the radial transport of particle, heat and momentum. The method used to determine the heat and particle transport coefficients is described in detail in the appendix. In summary, radially dependent particle, D_n, and electron heat, χ_e, diffusivities were optimized to reproduce the upstream electron density, n_e, and temperature, T_e, measured by Thomsom Scattering at the outer midplane (OMP). Ion heat diffusivity $\chi_i = \chi_e$ is assumed. Fig.'s 2b-g show the radial profiles of electron density and temperature, rotation, and the diffusivities used to produce them. These are expressed as a function of ψ_n, the normalized poloidal flux, which is by definition unity at the last closed flux surface and zero at the magnetic axis. The diffusivities show reduction in proximity to ψ_n=1, characteristic of the H-mode edge transport barrier.

In the far SOL the temperature diffusivity value becomes large due to the inverse dependence of radial temperature gradient in the diffusivity iteration method, and is typical of this method [19]. This undesirable result may be producing unrealistically high radial heat transport, with ~50% of the power crossing the separatrix reaching the far SOL B2.5 boundary shown in Fig. 2a. This value is similar for each of the four cases which are the focus of this paper as a result of using the same radial heat diffusivities. The appropriate value for the radial heat flux at this radial location is uncertain, given that the B2.5 grid boundary is artificial, the result of the limitations of the grid to non-shadowed regions of the plasma. However, more involved analysis of power balance in DIII-D typically indicates approximately 40% of the power crossing the separatrix reaches the target plates [20, 21], similar to the simulations presented here, indicating a realistic poloidal power flux. Regardless of these uncertainties, it is observed that these diffusivities produce satisfactory agreement with the upstream density, temperature, and rotation profiles, within the uncertainty of the experimental measurement.

The core boundary has a deuterium density boundary condition, adjusted to account for the different electron densities induced by the case-by-case variation of the carbon density at the core boundary. The density boundary conditions used, as well as the resulting core particle fluxes, are shown in Table II in the appendix. The input power at the core boundary (2.8 MW) was split equally between the ions and electrons.

In SOLPS, the radial flux of parallel ion momentum is expressed as a sum of two components, advective and diffusive (viscous):

$$\Gamma^m_{i,r} = m_i V_{\|i} \Gamma_{i,r} - m_i n_i \nu^{visc}_i \frac{\partial V_{\|i}}{\partial r} \quad (1)$$

Where $\Gamma^m_{i,r}$ is the radial flux of parallel ion momentum, m_i is the ion mass, $V_{\|i}$ is the parallel ion velocity, $\Gamma_{i,r}$ is the radial ion particle flux, and n_i is the ion density. ν^{visc}_i is the user-defined anomalous kinematic viscosity. It's noted here that this expression for radial momentum transport neglects any contribution from an inward momentum pinch, which could be significant to the overall radial momentum transport of the system [22, 23]. However, given the overall match to experimental density and rotation, the relevant physics appears to have been satisfactorily captured by the present simulation.

Within the radial momentum transport model employed by SOLPS, the anomalous radial viscosity pro-

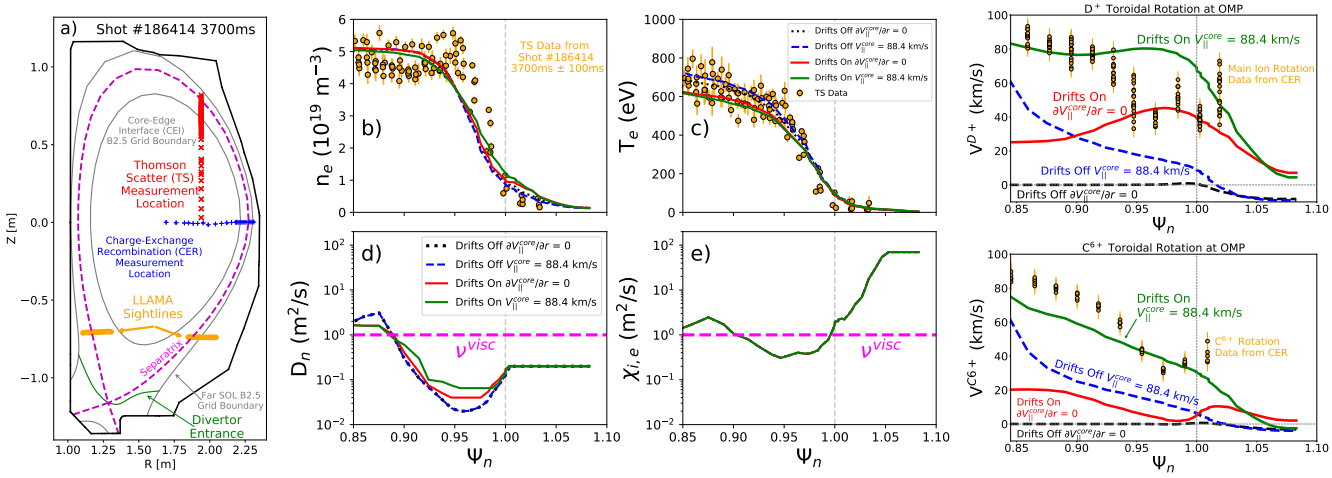

FIG. 2. a) Geometry of SOLPS domain and relevant diagnostics. Simulated b) n_e and c) T_e at the outer midplane compared to Thomson scattering data. The d) particle and e) heat diffusivities used to produce these radial profiles, with ν^{visc} shown as a horizontal dashed magenta line. f) Experimental outer midplane D^+ and g) C^{6+} toroidal velocity profile measured by CER, compared to the toroidal rotation for four simulations.

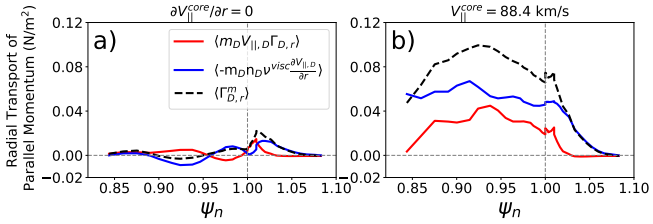

FIG. 3. Surface average, denoted via $\langle\rangle$, of radial transport of parallel momentum above the divertor entrance, with different parallel velocity boundary conditions at the CEI.

vides the only avenue for a velocity gradient to induce momentum transport. Physically, this represents the drag on radially adjacent flux tubes of different parallel velocity. For simplicity, the plasma viscosity is assumed constant across the radial domain, $\nu_i^{visc} = 1$ m^2/s. The value aligns with the expectation that ν_i^{visc} is between $0.4\chi_i$ and $1.5\chi_i$ [24] for ψ_n <1. As mentioned previously, χ can reach high values in the far SOL due to the low radial temperature gradient. Since radial variations in ν_i^{visc} are beyond the scope of the current analysis, ν_i^{visc} ~1 m^2/s is considered acceptable to prioritize the accuracy of core momentum transport, with potential inaccuracy in the far SOL. The sensitivity of results to ν_i^{visc} is discussed later.

Note that this momentum flux is one component of a larger momentum fluid equation solved by SOLPS. More thorough details are given for the equation in other publications [25–27]. The radial momentum transport, $\Gamma_{i,r}^m$ in a converged SOLPS simulation ultimately balances the momentum sources and fluxes from the other terms of this equation. However, the purpose of this Letter is to demonstrate how a radial flux of parallel momentum from the core can significantly alter the SOL flow asymmetry. This is actuated via different boundary conditions set in SOLPS.

A set of four simulations have been carried out, with different degrees of fidelity, with or without inclusion of particle drifts and with or without enforcement of a boundary condition for the parallel velocity at the inner radial boundary (core-edge interface, CEI, Fig. 2a), i.e $V_{||}^{core} = 88.4$ km/s, where 88.4 km/s is the rotation measured from Charge-Exchange Recombination (CER) spectroscopy at the CEI. This introduces a momentum flux at the core boundary which in steady state compensates for the other momentum sources and losses within the simulation. These other terms include $\Gamma_{i,r}^m$ and $\Gamma_{i,\theta}^m$ (radial and poloidal parallel momentum fluxes) at the B2.5 boundaries as well as the momentum source/sink terms within the plasma. Within these simulations the primary volumetric sources of momentum for the deuterium species are the friction and thermal forces as well as the interactions with the neutral species. When the $V_{||}^{core} = 88.4$ km/s boundary condition is not used, the core boundary institutes a zero velocity gradient condition, $\partial V_{||}^{core}/\partial r = 0$, allowing for non-zero parallel velocity but resulting in significantly reduced momentum flux (via elimination of the viscous momentum transport term in equation 1).

Fig.'s 2f and 2g compare the simulated D^+ and C^{6+} velocity at the outer midplane for the four simulations to measurements from CER. Even with the assumption of constant viscosity, by including drifts and using $V_{||}^{core}$=88.4 km/s, a reasonable agreement is achieved. Neglecting drifts or not providing the value of parallel velocity at the CEI results in substantial discrepancies in the rotation profile. Though disagreeing with the measured rotation, some self-generated D^+ SOL rota-

TABLE I. LFS peak J_{sat}, HFS/LFS divertor entrance integrated deuterium flux (D^+/s) and HFS/LFS peak Ly-α brightness for four simulations and experiment. Here, rotation "off" means $\partial V_{||}^{core}/\partial r = 0$ while "on" indicates $V_{||}^{core} = 88.4$ km/s.

Drifts / Rotation	LFS Peak J_{sat}	HFS/LFS Div. Entrance D^+ Flux	HFS/LFS Peak Ly-α Brightness
Off / Off	38.1	0.7	3.9
Off / On	28.4	1.5	5.2
On / Off	11.4	2.0	5.4
On / On	7.2	12.6	12.8
Experiment	7.8	-	8.6

tion is apparent from the presence of E×B drift flows alone (Fig. 2f, $\partial V_{||}^{core}/\partial r = 0$ curve). It is noted that, from past literature [16], this is expected of poloidal pressure asymmetries induced by the E×B flow. Fig. 3 shows how the surface averaged components of parallel momentum transport in Eq. 1 change with the use of the different parallel velocity boundary conditions. Momentum transport is seen to increase significantly with $V_{||}^{core}$=88.4 km/s, leading to greater near-SOL momentum (Fig 2f). A positive momentum flux, when projected to the poloidal plane, induces flow from the outer target to the inner target.

A synthetic diagnostic in SOLPS provides a comparison to the experimental Ly-α brightness just above the X-point. The comparison with the experimentally measured Ly-α signal is shown in Fig. 1a and Fig. 1b. Simulations without drifts underestimate the brightness at the HFS. When drifts are enabled without the $V_{||}^{core}$ boundary condition, the LFS Ly-α signal is over-estimated beyond the margin of error of the experimental data. However, the *asymmetry* of Lyman-α brightness is clearly affected by higher core rotation value with drifts enabled, indicating that parallel flow is an important physics mechanism driving this phenomenon. The target particle flux driving the neutral creation is shown in Fig. 1c and Fig. 1d, compared with Langmuir probe J_{sat} measurement for a discharge with similar parameters. The LFS particle flux is well reproduced once drifts are enabled with the appropriate value for parallel velocity at the core boundary. With $\partial V_{||}^{core}/\partial r$=0, the peak LFS J_{sat} is overestimated by 46%, while the $V_{||}^{core}$=88.4 km/s simulation underestimates the peak by 8%. The HFS particle flux is over-estimated for all cases presented here. This discrepancy may be due to a lack of detachment at the HFS target in the simulations, which is a common phenomenon in experiment known to reduce the target particle flux. This discrepancy may be caused by the chosen recycling coefficient of 0.98, though little change in this result was found by increasing recycling coefficient to 0.99, discussed later.

Fig. 4 shows the near-SOL ($\psi_n = 1.00 - 1.02$) flow towards the HFS is strongly enhanced by the inclusion of the $V_{||}^{core}$=88.4 km/s boundary condition at the core, largely driven by an increase in the relative contribution of the poloidal projection of parallel velocity ($V_{||,D,\theta} n_D$ in equation 2 in the appendix), compared with drift and Pfirsch-Schlüter components. The poloidal flux crossing the HFS divertor entrance is 4.0×10^{21} D^+/s in the case with drifts and $\partial V_{||}^{core}/\partial r$=0, increasing to 7.7×10^{21} D^+/s once $V_{||}^{core}$=88.4 km/s is applied. The ratio of the poloidal flux crossing the divertor entrance on the high field side to the poloidal flux on the low field side is 2.0 with the zero velocity gradient CEI condition, increased to 12.6 with $V_{||}^{core}$=88.4 km/s. These ratios are shown for all four cases in Table I.

Conversely, enabling drifts with $\partial V_{||}^{core}/\partial r$=0 results in more flow towards the LFS, with the stagnation of deuterium flow occurring higher upstream than it's $V_{||}^{core}$=88.4 km/s counterpart. This explains the observation noted from Fig. 1, that drifts alone significantly over-estimates both the LFS J_{sat} and Ly-α brightness. Note that Fig. 4 shows the stagnation of poloidal deuterium flow is near the LFS X-point (divertor entrance) with higher separatrix rotation, which aligns with previous results using a first-principle gyrokinetic code (XGC) [10]. Higher parallel velocity at the core without drifts is also seen to increase the flux toward the HFS, however not to the same levels as the full-fidelity simulation. This demonstrates the effect of combining drifts and core rotation, resulting in greater momentum transport to the SOL than either alone, as shown in Fig. 3.

The particle flux at the divertor entrance is amplified by the production of neutrals at the target. The subsequent ionization occurring within the divertor volume increases the local poloidal flux magnitude between divertor entrance and divertor target, as shown at the edges of Fig. 4. The HFS and LFS target deuterium ion fluxes, summed across SOL and PFR, are compared in Fig. 5. For these simulations, the SOL flux is an order of magnitude higher than the PFR flux. The HFS-LFS asymmetry of the target flux is increased with the addition of drifts and higher core rotation effects. The target flux asymmetry progresses from being nearly equal at the LFS and HFS targets (with drifts off and $\partial V_{||}^{core}/\partial r$=0), to the HFS experiencing approximately six times more deuterium ion flux with drifts on and $V_{||}^{core}$=88.4 km/s. Importantly, the target flux asymmetry responds to the combined effects of both drifts and rotation, as drifts on with zero core velocity gradient only had a HFS-LFS recycling ratio of 2 while higher rotation with drifts off had a recycling ratio of 1.5. This indicates that rotation of the confined plasma, an often ignored feature in fluid tokamak boundary modeling, has a significant effect on the prediction for target recycling asymmetry, especially when combined with drifts.

It is observed in these simulations that the flux due

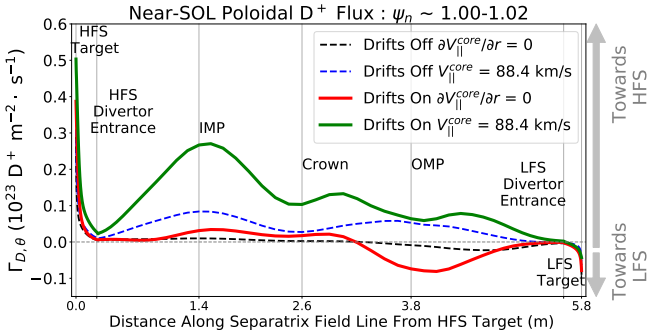

FIG. 4. Deuterium poloidal particle flux in the near-separatrix SOL for the four simulations.

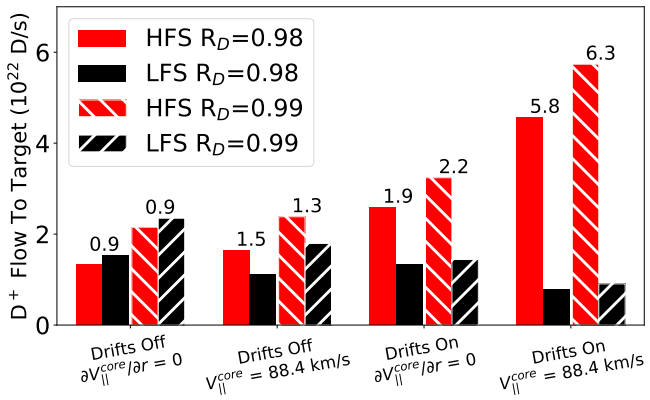

FIG. 5. Deuterium ion flow to the LFS and HFS targets. Numbers above the bars are the ratio of the HFS to LFS target particle flux.

to the poloidal projection of parallel velocity, $V_{||,D,\theta}n_D$ in equation 2 in the appendix, is the biggest driver of the target particle flux for both targets in all simulations and can be significantly larger than the E×B poloidal flux term, $V^E_{D,\theta}n_D$. By integrating the HFS target poloidal flux components for the two drift enabled cases, the ratio of $\int_{Tar}|V_{||,D,\theta}n_D|$ to $\int_{Tar}|V^E_{D,\theta}n_D|$ is 4.2 with $\partial V^{core}_{||}/\partial r$=0 and 4.4 with $V^{core}_{||}$=88.4 km/s. For the LFS target, this ratio is 2.9 with $\partial V^{core}_{||}/\partial r$=0 and 2.7 with $V^{core}_{||}$=88.4 km/s. Additionally, the different upstream rotation boundary conditions do not significantly change $V_{||}$ at the targets, with most of the change in the HFS-LFS particle flux asymmetry being driven by the changing HFS-LFS target deuterium density asymmetry. For example, with drifts, the peak deuterium $V_{||}$ at the HFS target only increases by 11% with $V^{core}_{||}$=88.4 km/s while the LFS decreases by 8%. This observation indicates that the three fold increase in recycling asymmetry is associated with the different fluxes at the divertor entrance, rather than a difference in the parallel velocities in the divertor or a change in the proportion of the terms at the target.

These results are partially dependent on the assumed recycling yield at the target. The recycling coefficient, R_D, is defined as the fraction of incoming particle flux which emits from the target as neutrals. In SOLPS, the wall recycling coefficient is user defined for each surface. Here, the recycling coefficient is assumed to be uniform, exploring asymmetric recycling coefficients is beyond the scope of the work presented here. In order to test the sensitivity of the conclusions to the choice of recycling coefficient, a second set of simulations was performed with R_D=0.99, raised from the value of 0.98, with no change in other input parameters. This effectively reduces the rate of deuterium pumping at the walls by a factor of two. Due to the density boundary condition at the CEI, this did not lead to significant changes in the upstream density or temperature. While a more comprehensive analysis could compare the results with consistent core particle fluxes, with radial particle diffusivity altered to re-match the upstream density, this is not done here. The CEI particle flux decreased by approximately 10-15% when the recycling was increased for all the cases considered. Conversely, the magnitude of the integrated target fluxes changed significantly, as is observed in Fig. 5. However, the asymmetry of the target particle flux i.e ratio of HFS recycling to LFS recycling, was robust against this change in recycling coefficient, generally the ratio was the same to within 7-20%. This indicates that the conclusion that upstream rotation leads to larger target flux *asymmetry* is not dependent on the recycling assumption of the simulations.

The user-defined anomalous viscosity was varied to understand its effect on the poloidal asymmetries. For this we focus on the case with drifts included and $V^{core}_{||}$=88.4 km/s, which has the largest viscous transport across the separatrix. In this case, lowering ν^{visc} to 0.4 m^2/s (from 1.0 m^2/s) increased the LFS deuterium flux by 28% and decreased the HFS flux by 5%, suggesting a greater effect on the LFS parameters. With the reduced ν^{visc} = 0.4, the ratio of HFS to LFS target flux decreased to 4.3, from 5.8 with ν^{visc} = 1.0 m^2/s. Reducing ν^{visc} to 0.05 m^2/s reduced the HFS to LFS target flux ratio to 3.7, indicating non-negligible contribution from the diffusive term in the radial momentum flux. Similarly to the target flux, an increase in the predicted Lyman-α brightness at the LFS is observed with reduced viscosity. However, only when the viscosity is lowered to ν^{visc} = 0.05 m^2/s, does the discrepancy grow significantly above the Lyman-α measurement uncertainty. The effect of rotation on divertor asymmetries is thus partially dependent on the plasma viscosity, though a range of viscosities produce agreement within measurement uncertainty of the Lyman-α signal.

In summary, the set of SOLPS-ITER simulations presented, based on an experimental scenario from the DIII-D tokamak, demonstrate that accounting for plasma ro-

tation results in stronger HFS-LFS asymmetries measured both at the divertor targets and across the boundary of DIII-D H-mode plasmas. With a realistic rotation profile in the simulation, momentum transport across the confined plasma boundary alters the upstream SOL flow structure, altering the flux of D^+ towards the divertor entrance. The poloidal flux across the divertor entrance is ultimately responsible for the strong asymmetry in the particle flux at the targets and, hence the recycled neutral source. The ratio of inboard/outboard target recycling was a factor of 1.9 with low momentum transport ($\partial V_{||}^{core}/\partial r$=0) and a factor of 5.8 with high momentum transport ($V_{||}^{core}$=88.4 km/s).

The large contribution of the poloidal projection of parallel velocity may surprise those familiar with the effect of drifts. Reversal of the E×B drift via reversal of the toroidal magnetic field have been known to strongly affect the target densities and thus detachment state of the plasma, with significant attention being paid to the PFR fluxes in past 2D edge modeling [4, 28]. However, rarely do these analyses consider the effect of toroidal rotation, at times explicitly setting toroidal rotation to zero at the core boundary [29]. It is clear that such a choice explicitly ignores the important contribution of upstream momentum transport to target recycling asymmetries. Higher separatrix rotation or higher viscosity scenarios may see a greater influence from parallel flow related terms than the modeled discharge due to larger SOL $V_{||}$. How this relationship extrapolates to future reactors, which are expected to have lower rotation [30], is left to future analysis.

This improved understanding of the interplay between core main ion rotation, and its indirect effect on SOL flows and target recycling, demonstrates the importance of including rotation profile comparisons in 2D edge modeling of tokamak plasmas. Going forward, accurate modeling of the radial momentum transport could be essential for accurately modeling divertor dynamics such as target detachment, where the spatial structure of recycling source has a key role, especially with regard to tightly baffled divertors. Given the necessity of detachment for future fusion reactors, this makes the momentum transport induced by the combination of drifts and rotation an important consideration for future reactor design.

ACKNOWLEDGEMENTS

We thank Adam McClean (Lawrence Livermore National Laboratory), Theresa Wilks (Massachusetts Institute of Technology), and Morgan Shafer (Oak Ridge National Laboratory) for helpful discussion of the simulations featured. This material is based upon work supported by the U.S. Department of Energy, Office of Science, Office of Fusion Energy Sciences, using the DIII-D National Fusion Facility, a DOE Office of Science user facility, under Award No.'s DE-AC02-09CH11466, DE-FC02-04ER54698, DE-SC0024523, DE-SC0014264, and DE-SC001930. Data included in figures and data required to reproduce simulation results are available from the author upon request. This report was prepared as an account of work sponsored by an agency of the U.S. Government. Neither the U.S. Government nor any agency thereof, nor any of their employees, makes any warranty, express or implied for the accuracy, completeness, or usefulness of any information, apparatus, product, or process disclosed, or represents that its use would not infringe privately owned rights. Reference herein to any specific commercial product, process, or service by trade name, trademark, manufacturer, or otherwise does not necessarily constitute or imply its endorsement, recommendation, or favoring by the U.S. Government or any agency thereof. The views and opinions of authors expressed herein do not necessarily state or reflect those of the U.S. Government or any agency thereof.

Appendix

A common technique used in interpretive modeling with SOLPS [19, 31] is to match the radial profiles of the plasma electron parameters (n_e and T_e) at the outer midplane via the iterative algorithm

$$D^{new} = -\Gamma^{SOLPS}/\nabla n_e^{exp}$$
$$\chi_{i,e}^{new} = q_e^{SOLPS} - \frac{5}{2}\Gamma T_e^{SOLPS}/n_e^{exp}\nabla T_e^{exp}$$

where Γ, q_e , and q_i are the particle flux, electron heat flux, and ion heat flux respectively. The superscripts "SOLPS" and "exp" designate the quantities that are taken from the computation and measurements. The code is run for several thousands of time steps ($\Delta t=10^{-5}$s) before the algorithm is ran again and new transport coefficients are determined.

Some discretion during the matching had to be exercised such that the diffusive transport coefficients did not grow unrealistically large. Large particle and heat transport coefficients lead to large particle and heat fluxes and thus unrealistically large neutral content or heat to the SOL boundary. With a core density boundary condition, the set of transport coefficients that reproduces a given density profile is non-unique, and thus even with a matching density the flux of particles from the core may be incorrect. An example of this effect can be seen by examining two cases from different points in the matching process, shown in Fig. 6. This figure shows that despite having a SOLPS profile within the spread of the Thomson scattering data, these two simulations led to different neutral content in the SOL. This has been documented in other profile matching exercises involving 2D edge codes as well [32].

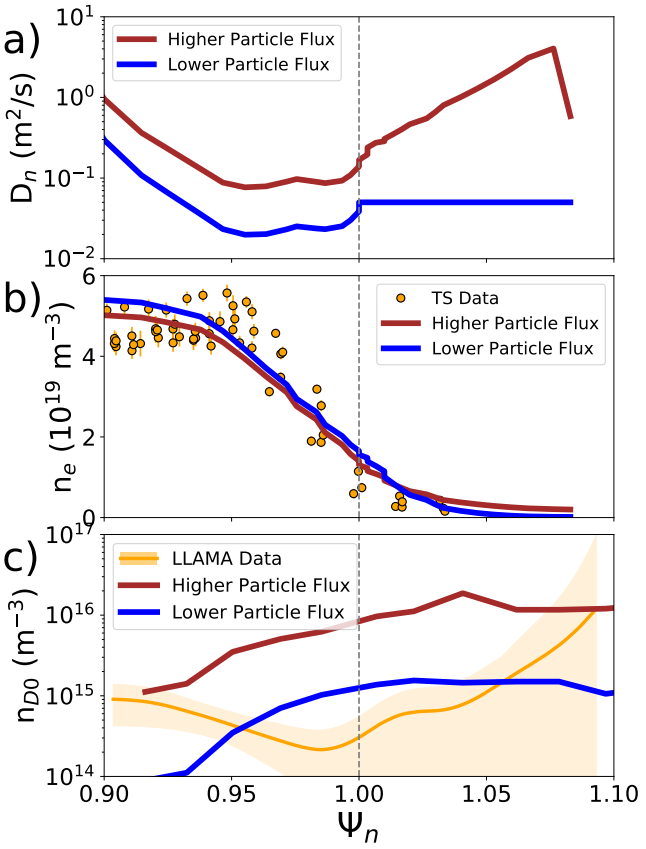

FIG. 6. Two cases with drifts off ($\partial V_{||}^{core}/\partial r = 0$) but with different profiles of a) D_n which give a similar b) n_e at the midplane but very different c) neutral density content in the simulation.

Once drifts were turned on, the profiles shifted considerably with the same anomalous radial particle transport diffusivity because drifts are a non-negligible component of the edge radial particle transport. The profiles were then re-matched by hand to achieve a match to the experimental data. This match is shown in Fig. 2b-e. Due to changing carbon content at the core boundary changing the electron density used for the matching process, the deuterium core-edge interface density boundary condition also had to be altered, values given in Table II. The upstream density likely also affects the SOL flows in these simulations [33], though an independent effect of density on HFS-LFS asymmetries is not explicitly considered here. It's also noted that for all four cases, the ionization within the SOLPS confined region was between 1.6×10^{21} - 2.0×10^{21}. Thus, there is some significant variation in the separatrix particle flux magnitude, though the main result of this article is the asymmetry of particle flux not so much the raw values.

Also given for ease of reference, the components of the SOLPS poloidal (thus target) particle flux in these simulations are

TABLE II. Deuterium density boundary conditions at the core-edge interface for the different cases considered, as well as the resulting radial deuterium particle flux at the interface. The boundary conditions were altered to match the electron density. Drifts on, $\partial V_{||}^{core}/\partial r = 0$ had a non-negligibly higher carbon content upstream, hence the lower required deuterium density boundary condition.

Drifts	Rotation BC	CEI Density (10^{19} D^+/m^3)	CEI Particle Flux (10^{21} D^+/s)
Off	$\partial V_{||}^{core}/\partial r = 0$	4.655	0.97
Off	$V_{||}^{core} = 88.4$ km/s	4.655	0.99
On	$\partial V_{||}^{core}/\partial r = 0$	3.400	1.7
On	$V_{||}^{core} = 88.4$ km/s	4.86	3.3

$$\Gamma_{D,\theta} = V_{||,D,\theta} n_D + V^E_{D,\theta} n_D - \Gamma^{PSch}_{D,\theta} + D_n \frac{\partial n_D}{\partial \theta} \quad (2)$$

Some of these terms were defined earlier. Note that θ here indicates the poloidal direction. The terms $\Gamma^{PSch}_{D,\theta}$ and $V^E_{D,\theta}$ terms are the poloidal Pfirsch-Schlüter flux (see [34, 35] for description and derivation) and poloidal E×B velocity respectively. $V_{||,D,theta}$ is the parallel deuterium velocity projected into the poloidal plane $\left(\frac{\vec{B}_\theta \cdot \vec{V}_{||,D}}{B}\right)$, n_D is the deuterium ion density, and D_n is the user defined diffusive particle transport coefficient. The relative importance of these terms is shown for two cases in Fig. 7.

It's noted here that the recycling coefficient value and distribution assumed, which directly affects the poloidal particle flux, varies significantly in past DIII-D analyses [36–40]. Carbon is assumed to absorb at any surface it comes into contact with (zero recycling). Carbon is brought into the simulation via physical and chemical sputtering. The Roth-Bohdansky model is used for physical sputtering while the chemical sputtering is given a flat 2% sputtering yield, which are standard assumptions in DIII-D SOLPS modeling [36, 41, 42]. Though spatially varying yields may produce a better match to the diagnostics, as suggested by other analyses [43], a dedicated attempt to match the carbon content of the simulation was not within the scope of this analysis. The separatrix midplane carbon content in SOLPS was found to be a factor of 1.6-4.8 higher than the measurement from CER.

[1] S. Mordijck, Nuclear Fusion **60**, 082006 (2020).
[2] A. Kirk, T. O'Gorman, S. Saarelma, R. Scannell, H. R. Wilson, and the MAST team, Plasma Phys. Control. Fusion **51**, 065016 (16pp) (2009).
[3] N. Wolf, T. Petrie, G. Porter, T. Rognlien, R. Groebner, and M. Mahdavi, Journal of Nuclear Materials **313-316**, 564 (2003).

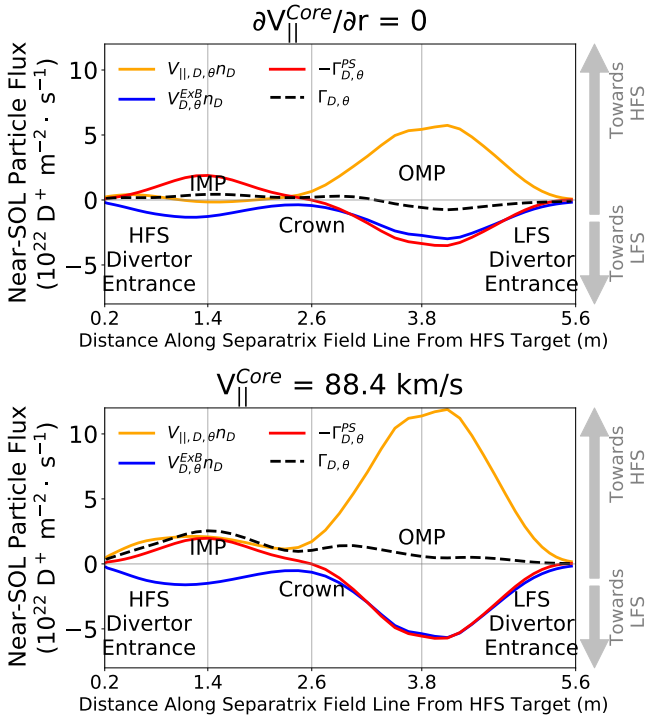

FIG. 7. The break down of components that go into equation 2 for the two drift enabled cases at R_D=0.98 and ν^{visc} = 1.0. The increased poloidal projection of parallel velocity, $V_{||,D,\theta} n_D$, causes more HFS directed flow, moving the stagnation of deuterium flow location closer to the LFS divertor entrance which is aligned with results from a first principles gyrokinetic code [10]

[4] A. Jaervinen, S. Allen, M. Groth, A. McLean, T. Rognlien, C. Samuell, A. Briesemeister, M. Fenstermacher, D. Hill, A. Leonard, and G. Porter, Nuclear Materials and Energy **12**, 1136 (2017).

[5] T. D. Rognlien, D. D. Ryutov, N. Mattor, and G. D. Porter, Phys. Plasmas **6**, 1851 (1999).

[6] P. C. Stangeby and A. V. Chankin, Nuclear Fusion **36**, 839 (1996).

[7] P. H. Diamond, S.-I. Itoh, K. Itoh, and T. S. Hahm, Plasma Phys. Control. Fusion **47**, R35 (2005).

[8] G. Kramer, A. Bortolon, A. Diallo, and R. Maingi, Nuclear Fusion **64**, 106035 (2024).

[9] A. V. Chankin and W. Kerner, Nuclear Fusion **36**, 563 (1996).

[10] G. Wilkie, F. Laggner, R. Hager, A. Rosenthal, S.-H. Ku, R. Churchill, L. Horvath, C. Chang, and A. Bortolon, Nucl. Fusion **64**, 086028 (2024).

[11] F. Laggner, A. Bortolon, A. M. Rosenthal, T. M. Wilks, J. W. Hughes, C. Freeman, T. Golfinopoulos, A. Nagy, D. Mauzey, and M. W. Shafer, Rev. Sci. Instrum. **92**, 033522 (2021), https://doi.org/10.1063/5.0038134.

[12] A. Rosenthal, J. W. Hughes, A. Bortolon, F. M. Laggner, T. M. Wilks, R. Vieira, R. Leccacorvi, E. Marmar, A. Nagy, C. Freeman, and D. Mauzey, Rev. Sci. Instrum. **92**, 033523 (2021).

[13] A. Bortolon, Ph.D. thesis, École Polytechnique Fédérale de Lausanne (2009), plasma Rotation and Momentum Transport Studies in the TCV Tokamak Based on Charge Exchange Spectroscopy Measurements.

[14] B. LaBombard, J. Rice, A. Hubbard, J. Hughes, M. Greenwald, J. Irby, Y. Lin, B. Lipschultz, E. Marmar, C. Pitcher, N. Smick, S. Wolfe, S. Wukitch, and the Alcator Group, Nuclear Fusion **44**, 1047 (2004).

[15] J. Rice, W. Lee, E. Marmar, P. Bonoli, R. Granetz, M. Greenwald, A. Hubbard, I. Hutchinson, J. Irby, Y. Lin, D. Mossessian, J. Snipes, S. Wolfe, and S. Wukitch, Nuclear Fusion **44**, 379 (2004).

[16] J. Loizu, P. Ricci, F. D. Halpern, S. Jolliet, and A. Mosetto, Physics of Plasmas **21**, 062309 (2014).

[17] J. A. Boedo, J. S. deGrassie, B. Grierson, T. Stoltzfus-Dueck, D. J. Battaglia, D. L. Rudakov, E. A. Belli, R. J. Groebner, E. Hollmann, C. Lasnier, W. M. Solomon, E. A. Unterberg, J. Watkins, and the DIII-D Team, Physics of Plasmas **23**, 092506 (2016).

[18] S. W. Reiter, D. Coster, B. Lipschultz, et al., Journal of Nuclear Materials **463**, 480 (2015).

[19] J. M. Canik, R. Maingi, S. M. Kaye, et al., Journal of Nuclear Materials **415**, S409 (2011).

[20] A. Leonard, C. Lasnier, J. Cuthbertson, T. Evans, M. Fenstermacher, D. Hill, R. Jong, W. Meyer, T. Petrie, and G. Porter, Journal of Nuclear Materials **220-222**, 325 (1995).

[21] C. Lasnier, S. Allen, A. Leonard, M. Mahdavi, T. Petrie, M. Rensink, and W. West, Nuclear Fusion **34**, 605 (1998).

[22] T. Hahm, P. Diamond, O. Gürcan, and G. Rewoldt, Physics of Plasmas **14**, 072302 (2007).

[23] C. Zimmermann, C. Angioni, R. McDermott, B. Duval, R. Dux, E. Fable, A. Salmi, U. Stroth, T. J. Tala, G. Tardini, T. Pütterich, and A. U. Team, Physics of Plasmas **31**, 042306 (2024).

[24] Y. Camenen, C. Angioni, A. Bortolon, B. Duval, E. Fable, W. Hornsby, D. N. R.M McDermott, Y. N. A. Peeters, and J. Rice, Plasma Physics and Controlled Fusion **59**, 034001 (2017).

[25] E. Sytova, E. Kaveeva, V. Rozhansky, I. Senichenkov, S. Voskoboynikov, D. Coster, X. Bonnin, and R. Pitts, Contributions to Plasma Physics **58**, 622 (2018).

[26] V. Rozhansky, E. Sytova, I. Senichenkov, I. Veselova, S. Voskoboynikov, and D. Coster, Journal of Nuclear Materials **463**, 477 (2015).

[27] V. Rozhansky, E. Kaveeva, P. Molchanov, I. Veselova, S. Voskoboynikov, D. Coster, G. Counsell, A. Kirk, S. Lisgo, and the ASDEX-Upgrade Team, Nuclear Fusion **49** (2009).

[28] A. V. Chankin, G. Corrigan, M. Groth, P. C. Stangeby, and J. contributors, Plasma Phys. Control. Fusion **57**, 095002 (2015).

[29] T. Rognlien, G. Porter, and D. Ryutov, Journal of Nuclear Materials **266-269**, 654 (1999).

[30] J. S. deGrassie, W. M. Solomon, J. E. Rice, and J.-M. Noterdaeme, Physics of Plasmas **23**, 082501 (2016).

[31] E. D. Emdee, R. J. Goldston, J. D. Lore, and X. Zhang, Nuclear Materials and Energy **27**, 101004 (2021).

[32] L. Horvath, B. Lomanowski, J. Karhunen, M. Maslov, P. Schneider, J. Simpson, M. Brix, B. Chapman-Oplopoiou, G. Corrigan, L. Frassinetti, M. Groth, K. Lawson, C. Maggi, S. Menmuir, R. M. amd D. Moulton, O. Myatra, D. Nina, T. Pereira, D. Réfy, S. Saarelma, M. Vécsei, and J. Contributors, Plasma Physics and Controlled Fusion **65**, 044003 (2023).

[33] L. Myllynen, Ph.D. thesis, Aalto University (2023), uEDGE predictions of SOL flows in DIII-D lower single-null L-mode plasma.

[34] V. Rozhansky, S. Voskoboynikov, E. Kaveeva, D. Coster, and R. Schneider, Nuclear Fusion **41**, 387 (2001).
[35] S. Hirshman and D. Sigmar, Nuclear Fusion **21**, 1079 (1981).
[36] X. Ma, H. Wang, H. Guo, A. Leonard, R. Maurizio, E. Meier, J. Ren, P. C. Stangeby, G. Sinclair, D. Thomas, R. Wilcox, J. Yu, and J. Watkins, Nucl. Fusion **62**, 126048 (2022).
[37] R. Maurizio, A. Leonard, A. McLean, M. Shafer, P. Stangeby, D. Thomas, and J. Yu, Nuclear Materials and Energy **34**, 101356 (2023).
[38] L. Casali, B. Covele, and H. Guo, Nuclear Materials and Energy **19**, 537 (2019).
[39] C. Sang, P. Stangeby, H. Guo, A. Leonard, B. Covele, L. Lao, A. Moser, and D. Thomas, Plasma Phys. Control. Fusion **59**, 025009 (2017).
[40] M. Groth, L. Owen, G. Porter, N. Brooks, M. Fenstermacher, W. Meyer, A. Leonard, T. Petrie, D. Rudakov, G. Wang, J. Watkins, and N. Wolf, Journal of Nuclear Materials **337-339**, 425 (2005).
[41] G. Sinclair, R. Maurizio, X. Ma, T. Abrams, J. Elder, H. Guo, D. Thomas, and A. Leonard, Nucl. Fusion **62**, 106024 (2022).
[42] J. Brooks, T. Sizyuk, G. Sinclair, and A. Hassanein, Nucl. Fusion **61**, 126071 (2021).
[43] M. Groth, G. D. Porter, M. E. Rensink, T. D. Rognlien, S. Wiesen, M. Wischmeier, T. Eich, A. Herrmann, S. Jachmich, C. J. Lasnier, H. W. Müller, J. G. Watkins, M. N. A. Beurskens, B. D. Bray, S. Brezinsek, N. H. Brooks, M. E. Fenstermacher, C. Fuchs, A. Huber, A. Kallenbach, A. W. Leonard, A. Meigs, D. L. Rudakov, et al., Journal of Nuclear Materials **415**, S530 (2011).